

# Nanostructured organic semiconductor films for molecular detection with surface-enhanced Raman spectroscopy

Mehmet Yilmaz<sup>1,2</sup>, Esra Babur<sup>1</sup>, Mehmet Ozdemir<sup>3</sup>, Rebecca L. Gieseking<sup>4</sup>, Yavuz Dede<sup>5</sup>, Ugur Tamer<sup>6</sup>, George C. Schatz<sup>4\*</sup>, Antonio Facchetti<sup>4,7\*</sup>, Hakan Usta<sup>3\*</sup> and Gokhan Demirel<sup>1\*</sup>

**$\pi$ -Conjugated organic semiconductors have been explored in several optoelectronic devices, yet their use in molecular detection as surface-enhanced Raman spectroscopy (SERS)-active platforms is unknown. Herein, we demonstrate that SERS-active, superhydrophobic and ivy-like nanostructured films of a molecular semiconductor,  $\alpha,\omega$ -diperfluorohexylquaterthiophene (DFH-4T), can be easily fabricated by vapour deposition. DFH-4T films without any additional plasmonic layer exhibit unprecedented Raman signal enhancements up to  $3.4 \times 10^3$  for the probe molecule methylene blue. The combination of quantum mechanical computations, comparative experiments with a fluorocarbon-free  $\alpha,\omega$ -dihexylquaterthiophene (DH-4T), and thin-film microstructural analysis demonstrates the fundamental roles of the  $\pi$ -conjugated core fluorocarbon substitution and the unique DFH-4T film morphology governing the SERS response. Furthermore, Raman signal enhancements up to  $\sim 10^{10}$  and sub-zeptomole ( $<10^{-21}$  mole) analyte detection were accomplished by coating the DFH-4T films with a thin gold layer. Our results offer important guidance for the molecular design of SERS-active organic semiconductors and easily fabricable SERS platforms for ultrasensitive trace analysis.**

The analysis of ultralow concentrations of (bio)chemical molecules is relevant in several fields including medicine, environmental science and homeland security<sup>1–3</sup>. Traditional approaches to molecular detection rely on optical, electrochemical, electronic and gravimetric methodologies<sup>4–7</sup>. Among these platforms, surface-enhanced Raman spectroscopy (SERS) is an ideal surface-sensitive technique allowing non-destructive molecular analysis with high sensitivity and selectivity approaching single-to-few molecule detection<sup>8,9</sup>. Although the exact enhancement mechanism in SERS remains questionable, two main theories are widely accepted<sup>9</sup>. The first and major contributor to the SERS enhancement factor (EF) is the electromagnetic mechanism, which mainly originates from the electric field magnification through excitation of localized surface plasmon resonances of the underlying SERS-active material. The second important SERS contributor is the chemical enhancement mechanism (CEM), which relies on the charge-transfer (CT) processes between the chemisorbed analyte molecules and the SERS-active material. Today, although the majority of high-performance SERS applications have relied on micro-/nanostructured metal coinage platforms<sup>8,9</sup>, the discovery of metal-free SERS platforms, enabled at large scale via cost/time-effective methods, is of great interest. In this respect, inorganic semiconductors such as TiO<sub>2</sub> (ref. 10), ZnO<sup>11</sup>, CuTe<sup>12</sup>, InAs/GaAs<sup>13</sup> and Cu<sub>2</sub>O<sup>14</sup> are promising, although limitations remain such as low performance and synthetic accessibility.

Organic films based on  $\pi$ -conjugated small molecular semiconductors (SMSs) offer unique advantages over their inorganic and macromolecular counterparts including structural versatility, facile and highly controllable synthesis and film fabrication, and fine-tuning of optoelectronic properties<sup>15–18</sup>. Metal-free SMS-based SERS may shed light on the poorly explored chemical enhancement mechanism since efficient charge/energy transfers between small molecules have impacted various applications including optoelectronics<sup>19,20</sup>, lasing<sup>21</sup>, chemical/biological-sensors<sup>22</sup> and medicine<sup>23</sup>. In addition, SMS films can be fabricated at a large scale by physical vapour deposition (PVD) as well as inexpensive printing methodologies, which could reduce production costs and enable great control of film morphological parameters<sup>24–26</sup>.

On the basis of the above-mentioned premises, we have recently pioneered the combination of a high-charge-carrier-mobility p-type (hole-transporting) organic semiconductor, C8-BTBT (Supplementary Fig. 1) with a thin vapour-deposited Au layer for SERS detection<sup>24</sup>. These results prompted us to question whether an n-type (electron-transporting) organic SMS would be a feasible option for SERS, how it would differ from C8-BTBT with regard to SERS detectivity, and whether further tuning of the analyte–SMS film interactions can be achieved by  $\pi$ -conjugated core substitution with fluorocarbon versus hydrocarbon chains. In this article, superhydrophobic, ivy-like nanostructured organic films are fabricated with an unprecedented SERS EF of  $>10^3$ , demonstrating

<sup>1</sup>Bio-inspired Materials Research Laboratory (BIMREL), Department of Chemistry, Gazi University, 06500 Ankara, Turkey. <sup>2</sup>Department of Bioengineering, Faculty of Engineering and Architecture, Sinop University, 57000 Sinop, Turkey. <sup>3</sup>Department of Materials Science and Nanotechnology Engineering, Abdullah Gül University, 38080 Kayseri, Turkey. <sup>4</sup>Department of Chemistry and the Materials Research Center, Northwestern University, 2145 Sheridan Road, Evanston, Illinois 60208-3113, USA. <sup>5</sup>Theoretical/Computational Chemistry Research Laboratory, Department of Chemistry, Gazi University, 06500 Ankara, Turkey. <sup>6</sup>Department of Analytical Chemistry, Faculty of Pharmacy, Gazi University, 06330 Ankara, Turkey. <sup>7</sup>Flexterra Inc., 8025 Lamon Avenue, Skokie, 60077 Illinois, USA. \*e-mail: g-schatz@northwestern.edu; a-facchetti@northwestern.edu; hakan.usta@agu.edu.tr; nanobiotechnology@gmail.com

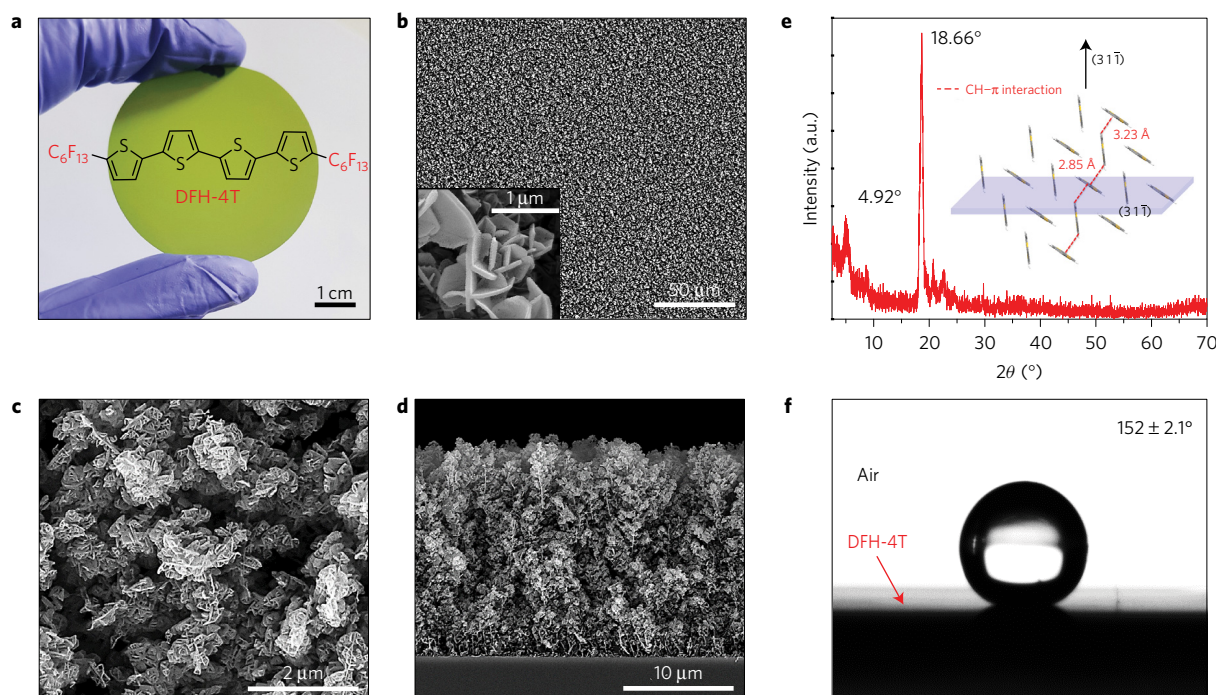


**Figure 1 | Characterization of nanostructured DFH-4T films.** **a**, Optical image of a vapour-deposited DFH-4T film (5 cm in diameter) with the chemical structure shown in the inset. **b–d**, Top-view (**b,c**) and cross-sectional (**d**) SEM images of nanostructured DFH-4T films. **e**, The  $\theta$ - $2\theta$  XRD pattern of a nanostructured DFH-4T film and the view of the molecular packing along the  $[3\ 1\ \bar{1}]$  crystal growth direction showing the dominant CH- $\pi$  interactions. **f**, Optical image of a water droplet on a nanostructured DFH-4T film used for contact-angle measurements.

that a metal-free organic small-molecule-based film can be SERS-active. The SMS used here is the fluorocarbon-substituted  $\alpha,\omega$ -diperfluorohexylquaterthiophene, DFH-4T (Fig. 1a), in which the  $\pi$ -electronic structure provides electron transport, while the perfluorohexyl ( $-n\text{-C}_6\text{F}_{13}$ ) chains enable excellent volatility for reliable and quantitative PVD film fabrication for highly uniform superhydrophobic films<sup>19,27</sup>. EF is further enhanced to  $\sim 10^{10}$  after coating of the superhydrophobic nanostructured DFH-4T film with a thin Au film, which allows sub-zeptomole ( $<10^{-21}$  mole) level analyte (methylene blue) detection. The combination of results comprising a molecular semiconductor similar to DFH-4T but without fluorocarbon substitution, DFH-4T platforms having different surface energies/morphologies, and molecular orbital computations provides insights into the key role of the DFH-4T molecular structure and film morphology affecting the SERS response.

### Fabrication of nanostructured DFH-4T films

DFH-4T was synthesized and purified according to the literature<sup>27</sup>. Nanostructured DFH-4T films ( $\sim 20\ \mu\text{m}$  thick) were prepared via PVD in  $\sim 10$  min on 5-cm-diameter Si(100) substrates using a  $90^\circ$  deposition angle, an ultrafast deposition rate of  $>40\ \text{nm s}^{-1}$ , and a short source–substrate distance of  $\sim 7$  cm under a  $\sim 10^{-6}$  torr vacuum (Fig. 1a). These substrates were maintained at  $\sim 30^\circ\text{C}$  so that thermally activated (diffusion) mass transport of the semiconductor molecules is limited across the substrate surface to further facilitate vertical crystal growth. These deposition parameters are preferred to slow, high-temperature, and large-distance vapour deposition, because they enable ballistic mass transport from the source to the substrate surface yielding rapid, uniform and reproducible crystal growth along the vertical direction<sup>28</sup>. Figure 1b–d reports scanning electron microscopy (SEM) images of DFH-4T films demonstrating the formation of mostly vertically aligned two-dimensional (2D) nanoplates ( $\sim 10$  nm thick) connected to a wire-like centre ( $\sim 150$  nm in diameter), thus yielding a unique 3D ivy-like uniform film morphology.

The DFH-4T film texturing was investigated by X-ray diffraction (XRD) measurements, and displays a major reflection at  $2\theta = 18.66^\circ$ , corresponding to a periodicity ( $d$ -spacing) of  $4.7\ \text{\AA}$  (Fig. 1e). Based on the film morphology dominated by nanoplates, this peak arises from the major crystalline phase along the nanoplate surface in the out-of-plane direction. Since the crystal structure of DFH-4T is known<sup>27</sup>, powder pattern simulation (Supplementary Fig. 2a) indicates that this peak originates from the  $(3\ 1\ \bar{1})$  diffraction planes, and the major intermolecular interactions governing the crystallization along the  $[3\ 1\ \bar{1}]$  direction are strong ‘CH- $\pi$ ’ contacts ( $\sim 2.85$ – $3.23\ \text{\AA}$ ) in DFH-4T herringbone packing (inset of Fig. 1e). The dominant molecular ordering across the nanoplate surface is further confirmed by the BFDH (Bravais–Friedel–Donnay–Harker) theoretical crystal morphology (Supplementary Fig. 2b), showing that the nanoplate 2D crystal plane grows almost perpendicular to the  $(3\ 1\ \bar{1})$  plane. In addition, a low-angle secondary reflection is observed at  $2\theta = 4.92^\circ$  ( $d$ -spacing =  $1.8\ \text{nm}$ ), which does not correspond to any simulated peaks, thus probably originating from the wire-like features observed along the film substrate normal. The corresponding  $d$ -spacing is far shorter than the DFH-4T molecular length ( $\sim 3.1\ \text{nm}$ ), suggesting that the molecules adopt a long-axis edge-on molecular orientation with a tilt angle of  $\sim 55^\circ$  from the substrate normal. Such molecular organization leads to the formation of isolated wire-like DFH-4T seeds, from which the nanoplates grows further. As evidenced from the cross-sectional SEM image (Fig. 1d), the rather weaker intensity of this reflection, as compared with that of the nanoplates, is consistent with the lower content of the former morphology across the semiconductor film. We believe that the combination of these growth features drives the formation of the DFH-4T film’s unique 3D ivy-like microstructure. DFH-4T film wettability was also studied by water contact-angle measurements, featuring a superhydrophobic surface (Fig. 1f) with a contact angle of  $\sim 152^\circ$  and a sliding angle of  $<1^\circ$  (surface energy =  $15\ \text{mJ m}^{-2}$ ), which is attributable to the combined presence of nanostructured

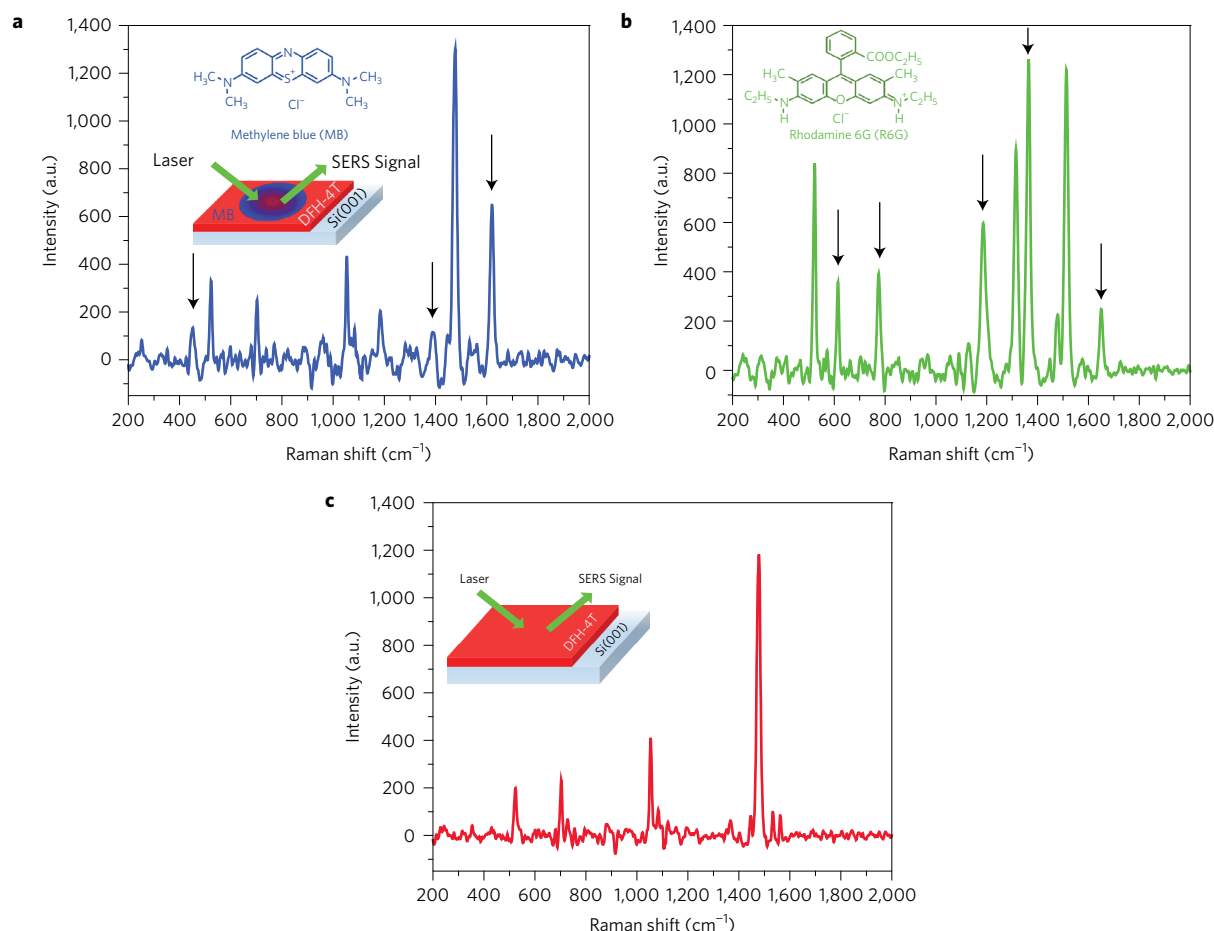


**Figure 2 | SERS response of nanostructured DFH-4T-based films.** **a,b**, SERS spectra of methylene blue (MB) (**a**) and rhodamine 6G (R6G) (**b**) on nanostructured DFH-4T films (insets show the chemical structure of MB/R6G and for each analyte molecule, characteristic Raman peaks are highlighted). **c**, Raman spectrum of a pristine DFH-4T film. Insets in **a,c** show the schematic representation of the corresponding SERS measurements.

organic surface and fluorocarbon functionalization in the molecular core.

### Raman enhancement for nanostructured DFH-4T films

The SERS characteristics of the pristine DFH-4T films were investigated by using methylene blue (MB) and rhodamine 6G (R6G) as Raman probes (Fig. 2a,b insets). In a typical experiment, 5  $\mu\text{l}$  of an aqueous analyte solution ( $1 \times 10^{-5}$  M) was placed on the DFH-4T/Si(001) platform resulting in contact angles of  $\sim 150^\circ$  for MB and  $\sim 149^\circ$  for R6G. Due to the superhydrophobic DFH-4T film surface, the analyte droplets preserve their spherical shape during solvent evaporation. Thus, after solvent removal, the MB and R6G molecules are confined into extremely small areas ( $\sim 200 \pm 30 \mu\text{m}$  in diameter), pointing to a beneficial hydrophobicity-enhanced concentration effect. This phenomenon is very different from common SERS platforms where contact angles of  $< 100^\circ$  promote spreading/wetting of the solution leading to spot areas of a few square millimetres (refs 24,25). Figure 2a,b shows the Raman spectra of MB and R6G, respectively, obtained on the pristine DFH-4T films at an excitation wavelength of 785 nm. While no Raman signals were recorded when  $10^{-5}$  M analyte solutions were deposited on bare Si(001) substrates (Supplementary Fig. 3), substantial Raman signals were collected for the same solutions when deposited on DFH-4T/Si(001), with a good signal-to-noise ratio and peak positions consistent with earlier reports (Supplementary Table 1)<sup>25,29,30</sup>. Note, DFH-4T film Raman spectra were also recorded to ensure that the SERS signals originate exclusively from the probe molecules (Fig. 2c). Remarkably, these results demonstrate that our

nanostructured DFH-4T film is an active SERS platform even in the absence of any noble metal, evidencing that organic small-molecule-based films can function as SERS platforms. The characteristic Raman peaks at  $1,621 \text{ cm}^{-1}$  for MB and at  $1,190 \text{ cm}^{-1}$  for R6G were selected to calculate the EFs of the DFH-4T film (see Supplementary Methods for details). Accordingly, EFs of  $3.4 \pm 1.3 \times 10^3$  for MB and  $6.7 \pm 2.1 \times 10^2$  for R6G were calculated ( $[\text{analyte}] = 1 \times 10^{-5}$  M), which are larger ( $\sim 100$ – $1,000\times$ ) than most inorganic semiconductor-based SERS platforms (Supplementary Table 2).

To evaluate whether the DFH-4T film's superhydrophobic nature, which could vary analyte solution spreading and molecular aggregation, is the origin of the large EFs, SERS experiments were performed by using MB solvent mixture solutions with gradually reduced surface tension. Thus, moving from water ( $72.9 \text{ mN m}^{-1}$ ) to ethanol ( $22.4 \text{ mN m}^{-1}$ ) mixture solutions progressively lowers the contact angle from  $\sim 150^\circ$  to  $\sim 54^\circ$  (Supplementary Fig. 4). Furthermore, a highly uniform MB film ( $\sim 200 \text{ nm}$ ) was also deposited via PVD (Supplementary Fig. 5). These depositions on DFH-4T films continue to lead to substantial EFs of  $\sim 2 \times 10^3$  for the ethanol solution and  $\sim 5.1 \times 10^2$  for the vapour-deposited MB film. The slight EF reduction compared with the pure water solution is probably due to increased spreadability of the low surface tension analyte solutions and, for the vapour-deposited MB film, incomplete conformal coverage/intimate contact of the DFH-4T surface with the analyte due to shadowing effects of the rough/3D structured DFH-4T film.

Considering that DFH-4T intrinsic carrier density is  $< 10^{13} \text{ carrier cm}^{-3}$ , Raman enhancement due to the electromagnetic



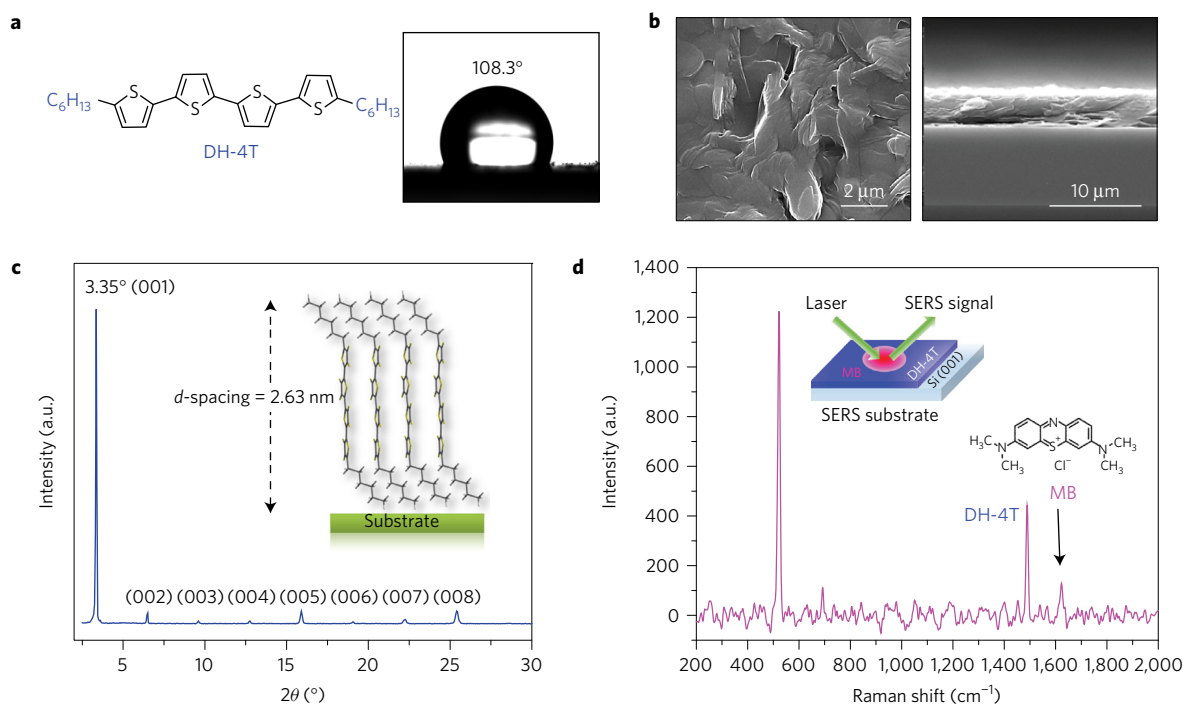


**Figure 3 | Characterization and SERS response of 2D DH-4T films.** **a**, The chemical structure of DH-4T and the optical image of a water droplet on a 2D DH-4T film used for contact-angle measurements. **b,c**, Top-view and cross-sectional SEM images (**b**) and  $\theta$ - $2\theta$  XRD pattern (**c**) of a 2D DH-4T film (inset depicts the view of the edge-on molecular orientation with a calculated  $d$ -spacing of 2.63 nm along the [001] film growth direction). **d**, SERS spectra of MB on pristine DH-4T film (inset shows the schematic representation of the SERS measurement).

mechanism is unlikely. Thus, the CEM might be responsible for the high EFs originating from favourable analyte/DFH-4T CT processes. Note that the EFs reported here are close to the largest predicted theoretically for the CEM<sup>31</sup>. The prominent SERS bands of MB at  $1,621\text{ cm}^{-1}$  ( $\nu(\text{C-C})$  ring stretches),  $1,391/1,433\text{ cm}^{-1}$  ( $\nu(\text{C-N})$  symmetric and asymmetric stretches), and  $450\text{ cm}^{-1}$  ( $\delta(\text{C-N-C})$  skeletal deformation mode) are slightly different from those observed on plasmonic metal surfaces (see below), further supporting the existence of the CEM since the analyte-specific binding geometry on the DFH-4T surface results in non-equivalent signal enhancements.

### Molecular and morphological origins of the SERS response

To understand the role of the DFH-4T molecular structure and unique film morphology on the SERS response, we investigated the films based on a structurally related small molecule, 5,5''-dihexyl-2,2':5',2'':5'',2'''-quaterthiophene (DH-4T, Fig. 3a) as well as pristine DFH-4T films having far smoother morphologies (Supplementary Fig. 6). DH-4T shares the same quaterthiophene  $\pi$ -conjugated backbone with DFH-4T, but it incorporates hydrocarbon ( $-n\text{-C}_6\text{H}_{13}$ ) instead of fluorocarbon ( $-n\text{-C}_6\text{F}_{13}$ ) substituents at the molecular termini as in DFH-4T. This molecule is a SMS exhibiting a field-effect charge carrier mobility (for holes) and frontier molecular orbital topologies similar to those of DFH-4T, but a  $\sim 0.4\text{ eV}$  higher energy for the frontier molecular orbitals<sup>32</sup>. DH-4T films, fabricated by PVD, consist of 2D (face-on oriented) highly interconnected plate-like grains (Fig. 3b), originating from the vertical molecular orientation on the substrate, as evidenced from XRD measurements (Fig. 3c). These films are substantially more hydrophilic (contact angle  $\sim 108.3^\circ$ , Fig. 3a) than those of DFH-4T (contact angle  $\sim 150^\circ$ ). Note, attempts to fabricate nanostructured/3D DH-4T films failed, highlighting the key role of fluorocarbon substitution to achieve the superhydrophobic morphology. When using MB as the molecular probe, the SERS enhancement factors on DH-4T are only  $8 \pm 2.0$  ([analyte] =  $1 \times 10^{-5}\text{ M}$ ) (Fig. 3d).

Furthermore, relatively smooth DFH-4T films were deposited via PVD by manipulating the deposition parameters (see Methods). This approach provides a 2D, plate-like film morphology with some out-of-plane crystal plates, but without ivy-like formations (Supplementary Fig. 6a). The contact angle of this surface ( $\sim 121^\circ$ ) is considerably smaller than that of the nanostructured DFH-4T surface ( $\sim 152^\circ$ ), due to morphological smoothening. SERS measurements with MB ( $10^{-5}\text{ M}$ ) reveal that, as compared with the nanostructured DFH-4T, the Raman signal intensity at  $1,621\text{ cm}^{-1}$  significantly decreases from  $\sim 750$  to  $\sim 21$  counts (Supplementary Fig. 6b) and the SERS enhancement factor significantly decreases to  $2 \pm 1.4$ .

Clearly, the above results indicate that both the molecular structure and film morphology play significant roles. Thus, a question that arises is the SERS origin in our nanostructured organic platform. As shown in Supplementary Fig. 7, our analytes do not exhibit any significant optical transitions at the laser excitation energy ( $1.58\text{ eV}$ ), neither in dilute solutions, nor in the solid state as pristine films on glass, nor when deposited on the DFH-4T film (onset absorption energies for MB =  $1.82\text{--}1.68\text{ eV}$  and R6G =  $2.15\text{--}2.05\text{ eV}$ ). In addition, DFH-4T films do not absorb at  $1.58\text{ eV}$ . Thus, the impressive EFs ( $10^2\text{--}10^3$ ) of our platform cannot be simply explained by resonant charge excitation processes on pristine analyte molecular aggregates or the nanostructured organic DFH-4T film. However, alternative energetically feasible processes may occur for hybridized analyte/DFH-4T electronic states at the analyte/semiconductor interface, very likely on the sharp rosette DFH-4T film edges, which eventually contributes to the magnification of Raman scattering cross-sections (see below).

### Quantum mechanical computations

To gain insights into the Raman enhancement mechanism in these systems, we have computed the excited-state properties and Raman spectra of complexes formed by the analyte (MB or R6G) and both DFH-4T and DH-4T (geometries shown in Supplementary Fig. 8 and molecular orbital energies shown in Supplementary Fig. 9) at

the INDO/SCI (intermediate neglect of differential overlap/single configuration interaction) level, which has rationalized the SERS enhancement mechanism on plasmonic metals<sup>33</sup>. For the DFH-4T-MB complex, the first excited state has an energy of 1.427 eV (869 nm) and a CT character as shown in Fig. 4a and Supplementary Fig. 10. Within computational error, this is close to the experimental SERS excitation energy (1.58 eV or 785 nm), given the simplifications of the INDO model, suggesting that resonance CT enhancement of the Raman signal is a likely source of the experimentally observed SERS. In contrast, replacing DFH-4T with DH-4T or changing MB to R6G tunes the CT state energy away from resonance with the photon energy, in line with the weaker Raman enhancements in these systems. Because of the limited wavefunction overlap between the two molecules, the oscillator strength of the CT state at 1.427 eV in the DFH-4T-MB complex is two orders of magnitude smaller than that of the first excited state of the MB molecule (see Fig. 4b and Supplementary Figs 11 and 12). Since the absorption into the CT state is so weak, it is reasonable that the experimental absorption near the SERS photon energy is too small to be observed, which again is consistent with our observations.

Despite the weak CT absorption, the computed Raman intensity of the characteristic vibrational mode of MB is strongly enhanced on resonance with the CT state. The high sensitivity of the CT state to molecular geometry allows this state to contribute strongly to the resonance differential polarizability even though its absorption is weak. The enhancement is also highly sensitive to the lifetime broadening,  $\Gamma$ , of the CT excited state, with enhancement factors of 20, 250 and 2,300 when  $\Gamma = 0.1$ , 0.05 and 0.025 eV, respectively, as shown in Fig. 4c and Supplementary Figs 13 and 14. Although the two smaller widths are smaller than has typically been used to compute resonance Raman intensities<sup>34,35</sup>, such narrow features have been observed for CT states in organic donor-acceptor co-crystals where the CT state is the lowest singlet excited state, with a width of 0.0125 eV measured in anthracene-PMDA crystals<sup>36</sup>. Thus, the presence of a narrow CT state, enabled by the highly textured DFH-4T substrate, is the key feature leading to the large enhancements observed experimentally. We note that the oscillator strengths at the INDO/SCI level are computed using a zero differential overlap approximation that may underestimate the oscillator strengths in the CT states; larger oscillator strengths would allow such large enhancements to occur with broader CT states.

Since the oscillator strength strongly depends on the substrate-analyte wavefunction overlap, these results also suggest that obtaining large enhancements is possible only for substrate morphologies that allow significant  $\pi$ -stacking of the analyte with the substrate molecules. Experimentally, we expect that the 3D nanostructured DFH-4T morphology has many crystal faces exposed, including those along the main crystalline direction ( $[3\ 1\ 1]$ ) (Fig. 1e and Supplementary Fig. 2b) that reveal quarterthiophene  $\pi$ -cores at different orientations to allow  $\pi$ -stacking with the analyte, whereas the 2D morphologies for DFH-4T and DH-4T primarily have fluoroalkyl and alkyl groups, respectively, exposed<sup>37</sup>. The key role of CT state absorption in the Raman enhancement is in line with our experimental observation that a 3D nanostructured DFH-4T morphology, as compared with its smoother 2D morphology, leads to a more effective chemisorption of the analyte molecules with proper molecular orientations to facilitate CT. We also note that the porous/shaped 3D morphology associated with DFH-4T would also provide larger electromagnetic enhancements (probably by a factor of  $\sim 10$ ) (ref. 38) than would occur for the 2D case due to the weak photonic resonance enhancement; however, this cannot be the dominant effect as it would lead to much larger intensities for DFH-4T than for MB, which is not what is observed in Fig. 2a.

These findings demonstrate that the DFH-4T 3D nanostructured morphology plays an important role in the CE mechanism via effective chemisorption of analyte molecules with proper molecular

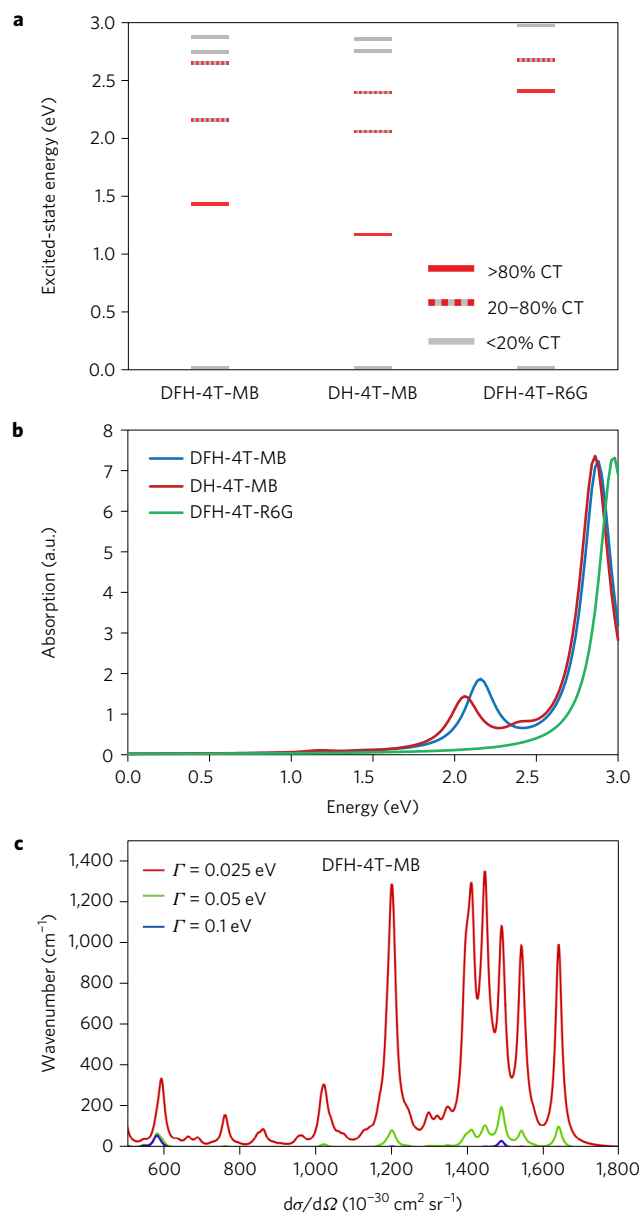


**Figure 4 | Quantum mechanical computations.** **a,b**, Computed excited-state energies (**a**) and absorption spectra (**b**) of substrate-acceptor complexes at the INDO/SCI level. **c**, Computed Raman spectrum of the DFH-4T-MB complex. The computation was performed with a photon energy of 1.427 eV at the INDO/SCI level, showing the effect of the lifetime broadening  $\Gamma$  on the Raman intensities.

orientations to facilitate CT between neighbouring substrate and analyte molecules. Critically, the electronic structure of the DFH-4T-MB system allows for a narrow CT feature on resonance with the photon energy, which enables strong Raman enhancement despite very weak absorption at these energies. The absence of the proper morphology (as in the 2D DFH-4T and DH-4T substrates) or of the proper energetic alignment (as for the DH-4T-MB and DFH-4T-R6G systems) accounts for the much weaker Raman enhancements observed in these systems.

### SERS investigation of Au-coated DFH-4T films

SERS has been widely employed in trace analysis of various (bio)chemical molecules<sup>1,3,39</sup>. To investigate whether further SERS enhancement is possible, DFH-4T films were coated with a thin (30 nm) Au film by PVD (Fig. 5a). SEM images reveal that the

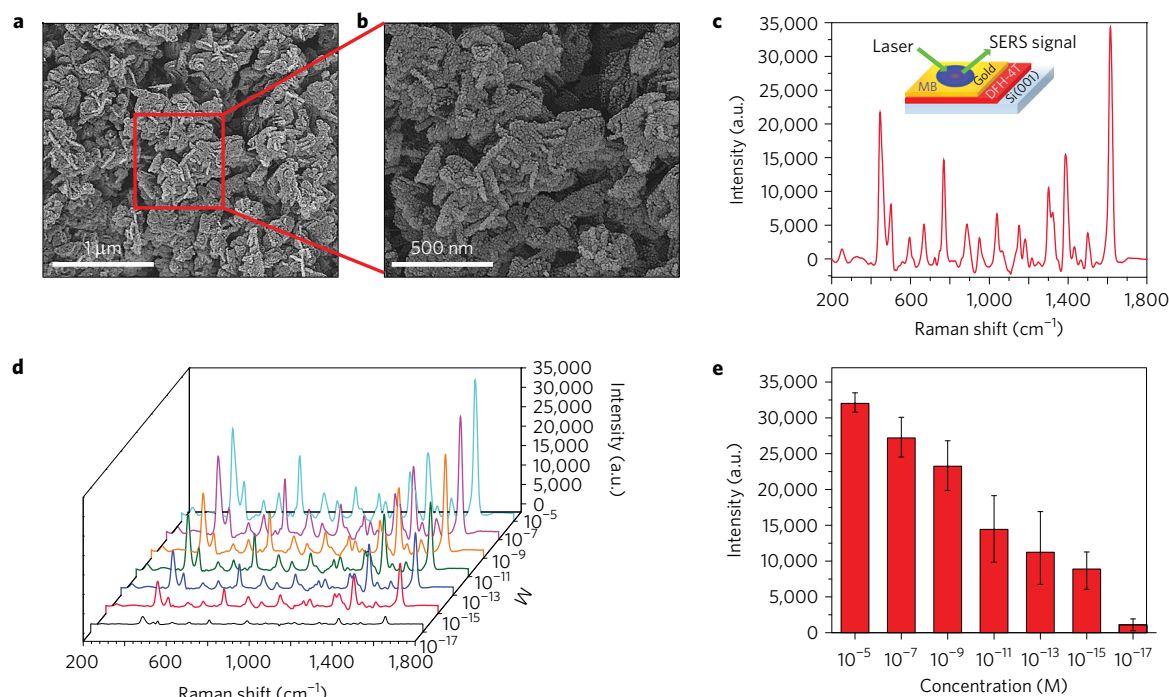


**Figure 5 | Characterization, SERS response and molecular detection of Au@DFH-4T films.** **a,b**, SEM images of Au-coated DFH-4T films at different magnifications. **c,d**, SERS spectra of MB on Au-coated DFH-4T films from a  $10^{-5}$  M concentration (**c**) (inset in **c** shows the schematic representation of the SERS measurement), and from a  $10^{-5}$ – $10^{-17}$  M concentration range (**d**). **e**, SERS intensities at  $1,621\text{ cm}^{-1}$  for MB concentration ranging from  $10^{-5}$  to  $10^{-17}$  M. The error bars indicate standard deviations from at least ten spectra for the MB concentrations of  $10^{-5}$ – $10^{-11}$  M and five spectra for the MB concentrations of  $10^{-13}$ – $10^{-17}$  M.

nanostructured superhydrophobic DFH-4T surface leads to the formation of closely packed Au particulates ( $\sim 9$ – $16$  nm in size, Fig. 5b), which can be attributed to the relative low binding energy and migration barrier of the gold atoms on the superhydrophobic surface<sup>40</sup>. When these Au@DFH-4T films were employed in SERS experiments with MB ( $1 \times 10^{-5}$  M), an EF of  $\sim 10^{10}$  for  $\nu = 1,621\text{ cm}^{-1}$  is obtained ( $\sim 35,000$  counts for Au@DFH-4T versus  $\sim 750$  counts for pristine DFH-4T films, Fig. 5c versus 2a). These EF values are among the highest values reported to date for the best nanostructured Au-based SERS platforms prepared by advanced top-down techniques such as electron-beam lithography, focused-ion beam, and photon lithography<sup>41</sup>. However, most importantly, this Au@DFH-4T platform can be fabricated easily by PVD over a large area (here to  $\sim 20\text{ cm}^2$ , limited by our equipment).

From morphological analysis, it is clear that the large SERS signal enhancement and good reproducibility are due to the combined DFH-4T/Au surface morphologies, promoting multiple hotspot generations, cavity resonances, and propagation of surface plasmon resonances<sup>42,43</sup>. Vertically aligned DFH-4T nanoplates combined with the plasmonic gold nanoparticles on top of them also provide tip-focusing effects, generating extremely high electric fields<sup>44</sup>. In addition, considering the interfaces and the energy levels in our DFH-4T–Au system, some energetically feasible CT processes may also play a critical role within the framework of the CE mechanism even for the Au@DFH-4T platform<sup>45–47</sup>.

The superhydrophobic nature of the Au@DFH-4T platform should enable molecular detection at ultralow concentrations. Figure 5d,e shows the SERS spectra of MB on Au@DFH-4T for deposition at different concentrations (from  $10^{-5}$  to  $10^{-17}$  M). All collected SERS spectra measured for  $10^{-5}$ – $10^{-15}$  M display high reproducibility in shape and peak positions, as exemplified in Supplementary Fig. 15 for the film resulting from a  $10^{-5}$  M concentration, with relative standard deviations ( $\text{RSD} \leq 0.11$ ) of the Raman band intensities at  $1,621\text{ cm}^{-1}$ ,  $1,394\text{ cm}^{-1}$  and

$449\text{ cm}^{-1}$ . For a concentration as low as  $10^{-17}$  M, the signal-to-noise ratio at  $\sim 1,621\text{ cm}^{-1}$ , when detected, remains  $> 8$ , indicating a sensitive platform for detecting sub-femtomolar concentrations. Note that  $5\text{ }\mu\text{l}$  of a  $10^{-17}$  M analyte solution corresponds to  $\sim 30$  MB ( $5\text{ }\mu\text{l} \times 10^{-17}\text{ M} \times N_A$ ) molecules deposited on the Au@DFH-4T surface, corresponding to a sub-zeptomole ( $< 10^{-21}$  mole) detection level. As shown in Fig. 5e, a linear relationship is also obtained between the Raman intensity and a broad MB concentration ( $10^{-5}$ – $10^{-17}$  M), demonstrating that following device engineering, our Au@DFH-4T platform holds promise for SERS detection even at a single-molecule level.

## Outlook

Ivy-like nanostructured DFH-4T films have been fabricated via PVD and employed as SERS-active platforms. Metal-free DFH-4T films show unprecedented Raman EFs ( $> 10^2$ – $10^3$ ) via a resonance CT mechanism between the DFH-4T substrate and the analyte. This mechanism, including the importance of the CT energetics and of the substrate morphology, was supported by comparative morphological experiments and electronic structure calculations. The combination of a superhydrophobic DFH-4T film with a plasmonic gold layer demonstrates remarkable Raman EFs ( $\sim 10^{10}$ ), and enables extremely low analyte detection ( $< 10^{-21}$  mole for MB). Our results provide important design rules for SERS-active  $\pi$ -conjugated organic semiconductor materials. Furthermore, they bring a new very promising entry for the fabrication of SERS-active nanostructured platforms enabling high chemical enhancements and few-to-single molecule level sensing without the need of expensive and time-consuming nano(micro)lithographic processes.

## Methods

Methods, including statements of data availability and any associated accession codes and references, are available in the [online version of this paper](#).



Received 14 December 2016; accepted 4 July 2017;  
published online 7 August 2017

## References

- Hudson, S. D. & Chumanov, G. Bioanalytical applications of SERS (surface-enhanced Raman spectroscopy). *Anal. Bioanal. Chem.* **394**, 679–686 (2009).
- Pearman, W. F. & Fountain, A. W. Classification of chemical and biological warfare agent simulants by surface-enhanced Raman spectroscopy and multivariate statistical techniques. *Appl. Spectrosc.* **60**, 356–365 (2006).
- Halvorson, R. A. & Vikesland, P. J. Surface-enhanced Raman spectroscopy (SERS) for environmental analyses. *Environ. Sci. Technol.* **44**, 7749–7755 (2010).
- Wang, L. *et al.* Simple, rapid, sensitive, and versatile SWNT-paper sensor for environmental toxin detection competitive with ELISA. *Nano Lett.* **9**, 4147–4152 (2009).
- Huang, N., Lü, T., Zhang, R. & Cao, W. High sensitivity gravimetric sensor made of carbon fiber epoxy composite on Pb ( $\text{Mg}_{1/3}\text{Nb}_{2/3}$ )  $\text{O}_3$ -PbTiO<sub>3</sub> single crystal substrate. *Appl. Phys. Lett.* **103**, 053507 (2013).
- Guo, X., Ying, Y. & Tong, L. Photonic nanowires: From subwavelength waveguides to optical sensors. *Acc. Chem. Res.* **47**, 656–666 (2013).
- Chen, A. & Chatterjee, S. Nanomaterials based electrochemical sensors for biomedical applications. *Chem. Soc. Rev.* **42**, 5425–5438 (2013).
- Schlücker, S. Surface-enhanced Raman spectroscopy: concepts and chemical applications. *Angew. Chem. Int. Ed.* **53**, 4756–4795 (2014).
- Lombardi, J. R. & Birke, R. L. A unified view of surface-enhanced Raman scattering. *Acc. Chem. Res.* **42**, 734–742 (2009).
- Alessandri, I. Enhancing Raman scattering without plasmons: unprecedented sensitivity achieved by TiO<sub>2</sub> shell-based resonators. *J. Am. Chem. Soc.* **135**, 5541–5544 (2013).
- Wang, Y. *et al.* Direct observation of surface-enhanced Raman scattering in ZnO nanocrystals. *J. Raman Spectrosc.* **40**, 1072–1077 (2009).
- Li, W. *et al.* CuTe nanocrystals: shape and size control, plasmonic properties, and use as SERS probes and photothermal agents. *J. Am. Chem. Soc.* **135**, 7098–7101 (2013).
- Quagliano, L. G. Observation of molecules adsorbed on III–V semiconductor quantum dots by surface-enhanced Raman scattering. *J. Am. Chem. Soc.* **126**, 7393–7398 (2004).
- Chen, L. Y., Yu, J. S., Fujita, T. & Chen, M. W. Nanoporous copper with tunable nanoporosity for SERS applications. *Adv. Funct. Mater.* **19**, 1221–1226 (2009).
- Facchetti, A.  $\pi$ -conjugated polymers for organic electronics and photovoltaic cell applications. *Chem. Mater.* **23**, 733–758 (2010).
- Labastide, J. *et al.* Directional charge separation in isolated organic semiconductor crystalline nanowires. *Nat. Commun.* **7**, 10629 (2016).
- Zhang, L. *et al.* Unconventional, chemically stable, and soluble two-dimensional angular polycyclic aromatic hydrocarbons: from molecular design to device applications. *Acc. Chem. Res.* **48**, 500–509 (2015).
- Zang, L., Che, Y. & Moore, J. S. One-dimensional self-assembly of planar  $\pi$ -conjugated molecules: adaptable building blocks for organic nanodevices. *Acc. Chem. Res.* **41**, 1596–1608 (2008).
- Capelli, R. *et al.* Organic light-emitting transistors with an efficiency that outperforms the equivalent light-emitting diodes. *Nat. Mater.* **9**, 496–503 (2010).
- Usta, H., Facchetti, A. & Marks, T. J. n-Channel semiconductor materials design for organic complementary circuits. *Acc. Chem. Res.* **44**, 501–510 (2011).
- Samuel, I. D. W. & Turnbull, G. A. Organic semiconductor lasers. *Chem. Rev.* **107**, 1272–1295 (2007).
- Roberts, M. E. *et al.* Water-stable organic transistors and their application in chemical and biological sensors. *Proc. Natl Acad. Sci. USA* **105**, 12134–12139 (2008).
- Kuribara, K. *et al.* Organic transistors with high thermal stability for medical applications. *Nat. Commun.* **3**, 723 (2012).
- Yilmaz, M. *et al.* Micro-/nanostructured highly crystalline organic semiconductor films for surface-enhanced Raman spectroscopy applications. *Adv. Funct. Mater.* **25**, 5669–5676 (2015).
- Yilmaz, M. *et al.* Combining 3-D plasmonic gold nanorod arrays with colloidal nanoparticles as a versatile concept for reliable, sensitive, and selective molecular detection by SERS. *Phys. Chem. Chem. Phys.* **16**, 5563–5570 (2014).
- Demirel, G., Malvadkar, N. & Demirel, M. C. Template-based and template-free preparation of nanostructured parylene via oblique angle polymerization. *Thin Solid Films* **518**, 4252–4255 (2010).
- Facchetti, A. *et al.* Building blocks for n-type molecular and polymeric electronics. Perfluoroalkyl- versus alkyl-functionalized oligothiophenes (nTs; n = 2–6). Systematic synthesis, spectroscopy, electrochemistry, and solid-state organization. *J. Am. Chem. Soc.* **126**, 13480–13501 (2004).
- Zhang, Y. *et al.* Intrinsic and extrinsic parameters for controlling the growth of organic single-crystalline nanopillars in photovoltaics. *Nano Lett.* **14**, 5547–5554 (2014).
- Akin, M. S. *et al.* Large area uniform deposition of silver nanoparticles through bio-inspired polydopamine coating on silicon nanowire arrays for practical SERS applications. *J. Mater. Chem. B* **2**, 4894–4900 (2014).
- Xu, W. *et al.* Surface enhanced Raman spectroscopy on a flat graphene surface. *Proc. Natl Acad. Sci. USA* **109**, 9281–9286 (2012).
- Sharma, B., Frontiera, R. R., Henry, A.-L., Ringe, E. & Van Duyne, R. P. SERS: materials, applications, and the future. *Mater. Today* **15**, 16–25 (January, 2012).
- Dinelli, F. *et al.* High-mobility ambipolar transport in organic light-emitting transistors. *Adv. Mater.* **18**, 1416–1420 (2006).
- Gieseke, R. L., Ratner, M. A. & Schatz, G. C. Theoretical modeling of voltage effects and the chemical mechanism in surface-enhanced Raman scattering. *Faraday Discuss.* <http://dx.doi.org/10.1039/C7FD00122C> (2017).
- Jensen, L., Zhao, L. L., Autschbach, J. & Schatz, G. C. Theory and method for calculating resonance Raman scattering from resonance polarizability derivatives. *J. Chem. Phys.* **123**, 174110 (2005).
- Jensen, L., Autschbach, J. & Schatz, G. C. Finite lifetime effects on the polarizability within time-dependent density-functional theory. *J. Chem. Phys.* **122**, 224115 (2005).
- Tokura, Y. & Koda, T. Experimental determination of the charge-transfer exciton band width in anthracene-PMDA crystal. *Solid State Commun.* **40**, 299–301 (1981).
- Facchetti, A. *et al.* Building blocks for n-type molecular and polymeric electronics. Perfluoroalkyl- versus alkyl-functionalized oligothiophenes (nT; n = 2–6). Part 2. Thin film microstructure, semiconductor performance, and modeling to charge injection in field-effect transistors. *J. Am. Chem. Soc.* **126**, 13859–13874 (2004).
- Zou, S. & Schatz, G. C. Silver nanoparticle array structures that produce giant enhancements in electromagnetic fields. *Chem. Phys. Lett.* **403**, 62–67 (2005).
- Fan, M. & Brolo, A. G. Silver nanoparticles self assembly as SERS substrates with near single molecule detection limit. *Phys. Chem. Chem. Phys.* **11**, 7381–7389 (2009).
- Pandey, P. A. *et al.* Physical vapor deposition of metal nanoparticles on chemically modified graphene: observations on metal-graphene interactions. *Small* **7**, 3202–3210 (2011).
- Ding, S.-Y. *et al.* Nanostructure-based plasmon-enhanced Raman spectroscopy for surface analysis of materials. *Nat. Rev. Mater.* **1**, 16021 (2016).
- Wei, W., Chen, K. & Ge, G. Strongly coupled nanorod vertical arrays for plasmonic sensing. *Adv. Mater.* **25**, 3863–3868 (2013).
- Doherty, M. D., Murphy, A., McPhillips, J., Pollard, R. J. & Dawson, P. Wavelength dependence of Raman enhancement of gold nanorod arrays: quantitative experiment and modelling of a hot spot dominated system. *J. Phys. Chem. C* **114**, 19913–19919 (2010).
- Ghenuche, P., Cherukulappurath, S., Taminiau, T. H., van Hulst, N. F. & Quidant, R. Spectroscopic mode mapping of resonant plasmon nanoantennas. *Phys. Rev. Lett.* **101**, 116805 (2008).
- Boeriger, C., Campana, R., Morabito, M. & Linic, S. Evidence and implications of direct charge excitation as the dominant mechanism in plasmon-mediated photocatalysis. *Nat. Commun.* **7**, 10545 (2016).
- Wang, X., Shi, W., She, G. & Mu, L. Using Si and Ge nanostructures as substrates for surface-enhanced Raman scattering based on photoinduced charge transfer mechanism. *J. Am. Chem. Soc.* **133**, 16518–16523 (2011).
- Lombardi, J. R. & Birke, R. L. Theory of surface-enhanced Raman scattering in semiconductors. *J. Phys. Chem. C* **118**, 11120–11130 (2014).

## Acknowledgements

This work was partially supported by Gazi University (grant no. 05/2015-19) and Polyera Corporation. G.D., H.U. and Y.D. acknowledge support from the Turkish Academy of Sciences, Distinguished Young Scientist Award (TUBA-GEBIP). A.F. thanks the Shenzhen Peacock Plan project (KQTD20140630110339343) and the BSF (AGMT-2012250//02).

## Author contributions

G.D., H.U. and A.F. conceived and designed the experiments. H.U., M.Ö. and A.F. synthesized the small molecular organic semiconductors. G.D., M.Y., U.T. and E.B. fabricated the nanostructured platforms and performed the experiments. G.C.S. and R.L.G. designed and performed the theoretical calculations. Y.D. helped with the density functional theory calculations. All authors discussed the results and co-wrote the paper.

## Additional information

Supplementary information is available in the [online version of the paper](https://doi.org/10.1038/nmat4957). Reprints and permissions information is available online at [www.nature.com/reprints](http://www.nature.com/reprints). Publisher's note: Springer Nature remains neutral with regard to jurisdictional claims in published maps and institutional affiliations. Correspondence and requests for materials should be addressed to G.C.S., A.F., H.U. or G.D.

## Competing financial interests

The authors declare no competing financial interests.

## Methods

**Fabrication and characterization of nanostructured DFH-4T films.** The synthesis and purification of  $\alpha,\omega$ -diperfluorohexylquaterthiophene (DFH-4T) and  $\alpha,\omega$ -dihexylquaterthiophene (DH-4T) were performed according to the reported procedure<sup>27</sup> and the resulting compounds were used as starting materials in vapour deposition. For fabrication, the silicon wafers (001 crystallographic orientation and 1–10  $\Omega$  resistivity) (5 cm in diameter) were sonicated in acetone for 10 min. The wafers were then washed with deionized water and dried under nitrogen gas flow. Afterwards, the samples were transferred to piranha solution. After 1 h, the samples were washed with deionized water and dried with nitrogen gas. To eliminate any contaminants, pre-cleaned samples were further treated with oxygen plasma at low pressure (0.2 mbar) for 30 min before the organic film deposition. In a typical deposition, DFH-4T or DH-4T powder (10–20 mg) was placed onto a tungsten boat and evaporated at about 250 °C under a fixed base pressure ( $1 \pm 0.2 \times 10^{-6}$  torr) in a slightly modified thermal evaporation system (NANOVAK HV) with a 90° deposition angle, and an ultrafast deposition rate ( $>40 \text{ nm s}^{-1}$ ) for varying deposition times (5–10 min) on cleaned silicon wafers. The difference between the organic material source and the substrate was kept at  $\sim 7$  cm. Note that for the fabrication of relatively smooth DFH-4T film, a slow deposition rate of  $0.2 \text{ Å s}^{-1}$  and large organic source–substrate distance of 20 cm were used during thermal evaporation. A thin layer of gold ( $\sim 30$  nm) was also deposited on the nanostructured and smooth DFH-4T films in the same system at a similar base pressure ( $1 \pm 0.2 \times 10^{-6}$  torr) to fabricate Au@DFH-4T films. The microstructure and morphology of films were analysed by a scanning electron microscope (FIE QUANTA 400F Field Emission SEM) and X-ray diffraction (XRD, Rigaku Ultima-IV X-ray diffractometer). UV–vis absorption and contact-angle measurements were performed on a Shimadzu 2600 UV–vis–near-IR spectrophotometer and a Krüss, DSA 100 drop shape analyser, respectively.

**SERS experiments.** A Delta Nu Examiner Raman Microscopy system equipped with a 785 nm laser source, a motorized microscope stage sample holder, and a cooled CCD (charge-coupled device) detector was used for all Raman studies. For all measurements,  $\times 20$  objective, 3  $\mu\text{m}$  spot size, 30 s acquisition time and 150 mW laser power were employed. The Raman enhancement ability of the deposited DFH-4T films with and without gold layer were investigated using methylene blue (MB) and Rhodamine 6G (R6G) as Raman probes. In a typical experiment, a certain volume of aqueous solution of MB or R6G probe molecules having different concentrations was placed on the fabricated films and allowed to dry. The final dried analyte spot shape and size was analysed by optical microscopy (Olympus SZX10 Stereo Microscope). The Raman spectra of samples from analyte concentrations of  $10^{-5}$ – $10^{-11}$  M were collected from at least ten different spots across the entire dried spot area, whereas the Raman spectra of samples from concentrations of  $10^{-13}$ – $10^{-17}$  were collected from at least ten measurements on spots at the periphery of the dried spot area (Supplementary Figs 16 and 17). Note, the Raman spectra of samples from concentration of  $10^{-17}$  M, when detected, are reproducible. For the purpose of enhancement factor calculations, we have employed the reference Raman spectra obtained from 0.1 M analyte concentrations of MB and R6G on the silicon substrate (Supplementary Fig. 3). The SERS enhancement factors (EFs) were calculated by utilizing the following equation and using the Raman intensity peak at  $1,621 \text{ cm}^{-1}$  for MB and  $1,190 \text{ cm}^{-1}$  for R6G:

$$\text{EF} = (N_{\text{Reference}} \times I_{\text{DFH-4T film}}) / (N_{\text{DFH-4T film}} \times I_{\text{Reference}})$$

where  $I_{\text{Reference}}$  and  $I_{\text{DFH-4T film}}$  are the Raman intensities of 0.1 M MB/R6G on the reference silicon substrate and  $10^{-5}$  M MB/R6G on the nanostructured DFH-4T film, respectively, and the  $N_{\text{Reference}}$  and  $N_{\text{DFH-4T film}}$  are the total number of MB/R6G molecules located in the laser spot area ( $7.065 \mu\text{m}^2$ ) on the reference silicon substrate and on the nanostructured DFH-4T film, respectively. It should be noted that all Raman measurements were carried out under identical experimental conditions (laser wavelength, laser power, microscope objective/lenses, spectrometer and so on). We calculated the average EF from the SERS substrate under the plausible assumption that all of the probe molecules within the laser spot are illuminated and contribute to the SERS spectra.

**Computational methodology.** The geometries and vibrational frequencies of the MB and R6G probe molecules and complexes of MB with DFH-4T and DH-4T molecules were computed using a density functional theory approach with the  $\omega$ B97X-D functional<sup>48,49</sup> and cc-pVTZ basis set<sup>50</sup>. This functional was selected because it is known to perform reasonably well for the delocalization and bond lengths of  $\pi$ -conjugated systems<sup>51</sup>. To reduce computational costs, the perfluorohexyl and hexyl substituents of DH-4T and DFH-4T, respectively, were replaced with perfluoroethyl and ethyl substituents. These calculations were performed using QChem 4.4 (ref. 52). All vibrational frequencies were scaled by the standard scaling factor of 0.956 for this level of theory<sup>53</sup>.

The excited-state energies were computed using a semiempirical intermediate neglect of differential overlap (INDO) Hamiltonian<sup>54</sup> in combination with a configuration interaction (CI) approach using single excitations (SCI). Because this approach is free of self-interaction error, it has been shown to accurately predict charge-transfer (CT) energies in several systems<sup>55,56</sup>. All possible single excitations within the INDO basis were generated, and the lowest 7,000 configurations were included in the CI matrix; this matrix was diagonalized to obtain the lowest 2,000 excited states. These calculations were performed using a code incorporating portions of MOPAC 7.1 (ref. 57) and the INDO/CI code from J. Reimers<sup>58</sup>.

The Raman intensities at the INDO/SCI level were computed using the  $\omega$ B97X-D/cc-pVTZ geometries, normal coordinates and vibrational modes using our recently implemented approach. The excited states were computed for geometries displaced by  $\pm 0.01 \text{ Å}$  along each vibrational mode, and the polarizabilities were computed using a sum-over-states approach summing over 2,000 excited states. The differential polarizabilities and Raman intensities were computed via numerical differentiation as has been previously described<sup>34</sup>.

**Data availability.** The data that support the findings of this study are available from the corresponding authors on reasonable request.

## References

- Chai, J.-D. & Head-Gordon, M. Long-range corrected hybrid density functionals with damped atom–atom dispersion corrections. *Phys. Chem. Chem. Phys.* **10**, 6615–6620 (2008).
- Chai, J.-D. & Head-Gordon, M. Systematic optimization of long-range corrected hybrid density functionals. *J. Chem. Phys.* **128**, 84106 (2008).
- Dunning, T. H. Jr Gaussian basis sets for use in correlated molecular calculations. I. The atoms boron through neon and hydrogen. *J. Chem. Phys.* **90**, 1007–1023 (1989).
- Körzdörfer, T., Parrish, R. M., Sears, J. S., Sherrill, C. D. & Brédas, J. L. On the relationship between bond-length alternation and many-electron self-interaction error. *J. Chem. Phys.* **137**, 124305 (2012).
- Shao, Y. *et al.* Advances in molecular quantum chemistry contained in the Q-Chem 4 program package. *Mol. Phys.* **113**, 184–215 (2015).
- Johnson, R. D. III NIST computational chemistry comparison and benchmark database. NIST Standard Reference Database Number 101 (2013); <http://cccbdb.nist.gov>
- Ridley, J. & Zerner, M. An intermediate neglect of differential overlap technique for spectroscopy: Pyrrole and the azines. *Theor. Chim. Acta* **32**, 111–134 (1973).
- Fox, T., Kotzian, M. & Rosch, N. Design of rigid donor–acceptor systems with a low-lying charge-transfer state. An INDO model study of barrelene-based compounds. *J. Phys. Chem.* **97**, 11420–11426 (1993).
- Nazeeruddin, M. K. *et al.* DFT-INDO/S modeling of new high molar extinction coefficient charge-transfer sensitizers for solar cell applications. *Inorg. Chem.* **45**, 787–797 (2006).
- Stewart, J. J. P. MOPAC: a semiempirical molecular orbital program. *J. Comput. Aided Mol. Des.* **4**, 1–105 (1990).
- Shapley, W. A., Reimers, J. R. & Hush, N. S. INDO/S parameters for gold. *Int. J. Quantum Chem.* **90**, 424–438 (2002).